J. Fluid Mech. (1980), *vol.* 101, *part* 2, *pp.* 281–306
Printed in Great Britain

Rotating barotropic flow over finite isolated topography

By PETER R. BANNON†

National Center for Atmospheric Research,‡ Boulder, Colorado 80307

(Received 17 August 1979 and in revised form 20 December 1979)

The flow of a rotating, incompressible fluid over isolated topography whose non-dimensional height (i.e. topographic height divided by the mean fluid depth) is large compared with the Rossby number is studied. Attention is restricted to flow which is sufficiently shallow that the free-surface equations provide an adequate description. The flow is forced laterally by a specified upstream inflow (obtained from solutions of the zonally symmetric model equations) and by a prescribed surface stress. Dissipation is incorporated using a Rayleigh friction acting anti-parallel to the flow.

Steady-state solutions for uniform inflow on an f-plane are found for (*a*) linear viscous flow, (*b*) quasi-geostrophic flow with and without friction and (*c*) inviscid flow with and without a rigid lid. The presence of friction produces an upstream–downstream flow asymmetry over the obstacle and an associated topographic drag while inertial terms produce left–right (relative to an observer looking downstream) asymmetry. The blocking efficiency B (the percentage of the incident mass flux going around the obstacle rather than over it) of a Gaussian obstacle is largest ($\sim 100\%$) for case (*a*) when viscous effects are small. In contrast quasi-geostrophic theory calculates no flow blocking ($B \equiv 0$). For inviscid inertial theory, $B \sim 10\%$ and is independent of the Rossby number. The presence of a free surface decreases the blocking for small-Rossby-number flow.

Numerical solutions of the appropriate initial, boundary-value problem for the complete model equations confirm these results and extend them to include the effects of (i) horizontal shear in the upstream inflow, (ii) the magnitude and shape of the topography, and (iii) variations in the Coriolis parameter (β-effect).

1. Introduction

Hide (1961) advanced the hypothesis that the Great Red Spot of Jupiter is the result of topographic blocking of a flow in a rapidly rotating fluid. Hide argued that dynamical constraints on the flow, as first deduced theoretically by Proudman (1916) and Taylor (1921), and demonstrated in the laboratory by Taylor (1923), will lead to the formation of a stagnant body of fluid above an (assumed) Jovian obstacle with two-dimensional flow around the obstacle. Hide named this phenomenon a Taylor column.

Though Hide's original hypothesis is subject to scientific debate (see, for example, Stone & Baker 1968, and Hide 1971), evidence for the existence of Taylor columns has

---

† Present affiliation: Department of the Geophysical Sciences, University of Chicago, Chicago, Illinois 60637 U.S.A.

‡ The National Center for Atmospheric Research is sponsored by the National Science Foundation.

0022-1120/80/4620-2600 $02.00 © 1980 Cambridge University Press

been presented for other geophysical fluid flows. Most notable have been contributions in oceanography. Hogg (1973*b*), Roberts *et al.* (1974), and Huppert & Bryan (1976) have interpreted observations over seamounts as being consistent with the presence of Taylor columns. In contrast no Taylor columns have been documented in the earth's atmosphere. However, the Taylor column mechanism has been invoked as an aid in understanding the airflow over the Alps (Buzzi & Tibaldi 1977) and over the Tibetan plateau (Nakamura 1978). The fundamental importance of the Taylor column lies in the fact that it is the premier example of the deflexion by rotational effects of flow around rather than over a topographic feature.

The first theoretical study of a Taylor column was that of Jacobs (1964) who presented a steady, linear, viscous analysis. In such a model, vertical velocities associated with flow over the obstacle are counteracted by Ekman pumping in the boundary layer to produce a stagnant region when the non-dimensional slope is $O(1)$. However, the theory, which predicts upstream–downstream and left–right† symmetry for symmetric obstacles, is not in agreement with laboratory simulations (Hide & Ibbetson 1966).

In an attempt to remove this deficiency, Ingersoll (1969) formulated an inviscid model using steady quasi-geostrophic theory. Such an approach is well-posed provided the flow possesses no closed streamlines. Ingersoll gave a heuristic argument based on vanishingly small viscosity to obtain the boundary condition of zero tangential velocity on closed streamlines. The theory predicts the formation of a Taylor column to the right of the obstacle, in agreement with laboratory simulations. However, the specification of both the stream function and its normal derivative about the column is an overspecification of the appropriate elliptic equation.

Since then quasi-geostrophic theory has been extended to include the effects of horizontal shear (Cottrell 1970), friction (Vaziri & Boyer 1971), stratification (Hogg 1973*a*), and variable Coriolis parameter (McCartney 1975). The problem of closed streamlines was still not solved, however. Another shortcoming of the quasi-geostrophic approach is that the theory is limited to consideration of topography whose non-dimensional height (i.e. topographic height divided by the mean fluid depth) is of the order of the Rossby number. Huppert (1975) has shown that closed streamlines (i.e. Taylor columns) form only for topography which is several times the Rossby number. This result is valid in the limit of vanishing Rossby number (and hence topography).

Johnson (1978*a*) considered the inviscid, time-dependent problem and obtained a variational principle to describe steady motions at finite Rossby number over obstacles of finite height. He extended Huppert's (1975) criterion for the formation of a Taylor column and showed it to be an underestimate for finite Rossby number. In addition he found that for certain flow initiations, a Taylor column will exist over the obstacle as well as a smaller, more intense vortex of opposite sign to the right. Solutions for this vortex pair, however, were presented only in the quasi-geostrophic limit.

The purpose of the present study is to investigate the effect on the fluid flow of obstacles whose non-dimensional height is large compared with the Rossby number. Such an investigation extends quasi-geostrophic results beyond the point where closed

---

† In this paper left and right are with respect to an observer looking downstream (upstream) for counterclockwise (clockwise) rotation.

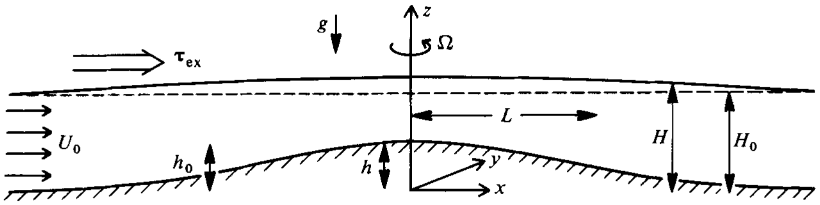

FIGURE 1. Schematic illustration of the model geometry depicting a cross-section along the x axis. Peak of the Gaussian obstacle lies at the origin.

streamlines form. In addition the effects of finite Rossby number, viscosity, horizontal shear of the inflow, variation of the Coriolis parameter with latitude, and presence of a free surface are ascertained. Emphasis is placed on determining how much flow goes around rather than over a single isolated topographic feature.

The model consists of the barotropic free surface equations on an f or β-plane. The flow is forced laterally by a specified upstream inflow (obtained from solutions of the zonally symmetric equations) and by a distribution of surface stress. This inviscid set of equations with no forcing has been integrated numerically by Kasahara (1966), Vergeiner & Ogura (1972), and Edelmann (1972) over a channel domain with rigid, left–right and periodic, upstream–downstream boundaries. Such an approach does not enable the horizontal structure of the flow incident on the obstacle to be adequately controlled by the experimenter. Moreover, no author was able to achieve a steady state. Here dissipation is incorporated using a Rayleigh friction acting anti-parallel to the flow. The modified set is integrated to a steady state over a rectangular domain with open boundaries on all four sides.

In the next section, the model assumptions are delineated, the basic equations presented, and the numerical model used in solving the initial, boundary-value problem is described. Section 3 presents exact steady-state solutions of the model equations for linear, viscous flow. In §4 quasi-geostrophic results are reviewed for flow with and without friction. Section 5 extends quasi-geostrophic theory to finite Rossby number with steady-state solutions for inviscid flow with and without a rigid lid. Section 6 presents the results of numerical integrations of the initial, boundary-value problem for a variety of flow parameters. The paper concludes with a section summarizing the results.

It should be noted that not all the results presented here are new (e.g. §§3 and 4). Their inclusion, however, will facilitate comparison with the numerical results of §6 and provide a comprehensive survey of rotating barotropic flow over topography.

2. The model

2.1. *Basic equations*

We consider the flow of a rotating incompressible fluid over a single topographic feature located at the origin of a Cartesian co-ordinate system (x, y, z). Figure 1 summarizes the model geometry. The obstacle's height $h = h(x,y)$ has a maximum value h_0 and falls to $\frac{1}{2}h_0$ in a horizontal distance L. The obstacle is isolated in that $h \rightarrow 0$ as $r = (x^2+y^2)^{\frac{1}{2}} \rightarrow \infty$. The fluid has a free surface of height H. A gravitational force $-g\hat{z}$ acts to restore that surface to its unperturbed height H_0. The rotation vector is

Symbol	Definition	Name
ϵ	U_0/fL	Rossby number
γ	κ/fH_0^2	Ekman number
γ_R	R/fH_0	Rayleigh–Ekman number
δ	H_0/L	aspect ratio
μ	h_0/H_0	topographic parameter
λ	f^2L^2/gH_0	rotational Froude number
$\hat{\beta}$	$\beta L^2/U_0$	beta parameter

TABLE 1. Non-dimensional flow parameters.

$\Omega\hat{\mathbf{z}} = \frac{1}{2}(f+\beta y)\hat{\mathbf{z}}$. The fluid has density ρ and (constant) kinematic viscosity κ. Far upstream ($x = -\infty$) a flow of characteristic speed U_0 is incident on the obstacle. The fluid is driven by a mass flux in the y direction or by an externally applied surface stress $\boldsymbol{\tau}_{\mathrm{ex}}$. The fluid velocity relative to the rotating frame is (u, v, w), P denotes the sum of the fluid pressure and the potential of the conservative body forces, and t time.

It is convenient to introduce the following non-dimensional quantities denoted by asterisks.

$$\left.\begin{array}{ll} \mathbf{v} = U_0(u^*, v^*), & w = U_0\dfrac{H_0}{L}w^*, \\ (x,y) = L(x^*,y^*), & z = H_0 z^*, \\ t = \dfrac{L}{U_0}t^*, & (f+\beta y) = f\left(1+\dfrac{\beta L y^*}{f}\right), \\ h = h_0 b^*, & H = H_0(1+s^*), \\ P = \rho g H_0 - \rho g z + \rho U_0 f L p^*, & \boldsymbol{\tau}_{\mathrm{ex}} = \rho R U_0 \boldsymbol{\tau}^*. \end{array}\right\} \tag{2.1}$$

Though the time-dependent equations (see below) are solved, attention is confined to steady-state solutions. Thus use of the advective time scale L/U_0 is appropriate. In the scaling of the surface stress $\boldsymbol{\tau}_{\mathrm{ex}}$, a constant Rayleigh friction speed R has been introduced.

The non-dimensional Navier–Stokes equations are, dropping the asterisks,

$$\epsilon\frac{\mathcal{D}u}{\mathcal{D}t} - (1+\hat{\beta}\epsilon y)v = -\frac{\partial p}{\partial x} + \gamma\Delta u, \tag{2.2a}$$

$$\epsilon\frac{\mathcal{D}v}{\mathcal{D}t} + (1+\hat{\beta}\epsilon y)u = -\frac{\partial p}{\partial y} + \gamma\Delta v, \tag{2.2b}$$

$$\delta^2\epsilon\frac{\mathcal{D}w}{\mathcal{D}t} = -\frac{\partial p}{\partial z} + \delta^2\gamma\Delta w, \tag{2.2c}$$

$$\frac{\partial u}{\partial x} + \frac{\partial v}{\partial y} + \frac{\partial w}{\partial z} = 0, \tag{2.2d}$$

where

$$\frac{\mathcal{D}}{\mathcal{D}t} \equiv \frac{\partial}{\partial t} + v.\nabla + w\frac{\partial}{\partial z},$$

$$\Delta \equiv \frac{\partial^2}{\partial z^2} + \delta^2\nabla^2,$$

and ∇ is the horizontal component of the gradient operator. Non-dimensional parameters are denoted by lower case Greek letters and defined in table 1.

The vertical boundary conditions are:

(i) kinematic condition at the free surface,

$$w(z = 1+s) = \left(\frac{\partial}{\partial t}+\mathbf{v}\,.\nabla\right)s; \tag{2.3a}$$

(ii) the lower boundary is impermeable,

$$w(z = \mu b) = \mathbf{v}\,.\nabla(\mu b); \tag{2.3b}$$

(iii) the pressure is continuous at the free surface (effects of surface tension are assumed negligible),

$$P(z = 1+s) = 0; \tag{2.3c}$$

(iv) the surface stress is continuous at $z = 1+s$,

$$\gamma_R \boldsymbol{\tau} = \gamma \left.\frac{\partial \mathbf{v}}{\partial z}\right|_{1+s}; \tag{2.3d}$$

(v) no-slip constraint at $z = \mu b$,

$$\mathbf{v}\times\hat{\mathbf{N}} = 0, \tag{2.3e}$$

where $\hat{\mathbf{N}}$ is a unit vector normal to the bottom surface.

In this study, the range of the parameters in table 1 is assumed to be

$$(\delta,\gamma) \ll 1, \tag{2.4a, b}$$

$$(\epsilon,\mu,\lambda,\hat{\beta}) \lesssim 1, \tag{2.4c}$$

and γ_R is discussed below. Geometrically the fluid is taken to be shallow: $L \gg H_0$. This feature is characteristic of many large-scale geophysical flows. It provides constraint (2.4*a*) that the aspect ratio is small. The constraint (2.4*b*) that the Ekman number is small restricts viscous effects to thin boundary layers. The topography is allowed to be a significant fraction of the mean fluid depth: $h_0 \lesssim H_0$. In contrast to (2.4), quasi-geostrophic theory assumes

$$(\mu,\gamma^{\frac{1}{2}}) \lesssim \epsilon \ll 1, \tag{2.5a, b}$$

$$(\delta,\lambda,\hat{\beta}) \lesssim 1, \tag{2.5c}$$

so that the fluid may be thick but is rapidly rotating while the topography is weak.

As $\delta^2 \to 0$, (2.2) indicates that the flow becomes hydrostatic ($\partial p/\partial z = 0$) and laterally inviscid. Pressure continuity (2.3*c*) is then satisfied provided

$$s = \lambda\epsilon p. \tag{2.6}$$

The result that the horizontal pressure gradients are independent of z suggests that the vertical shear is small. An estimate of the magnitude of the vertical shear may be obtained using, for example, the equation describing the y component of vorticity. It may be formed from (2.2) in the usual manner. The result is

$$\epsilon\frac{\mathscr{D}}{\mathscr{D}t}\left(\frac{\partial u}{\partial z}-\delta^2\frac{\partial w}{\partial x}\right) = (1+\hat{\beta}\epsilon y)\frac{\partial v}{\partial z}-\epsilon\left(\frac{\partial u}{\partial z}-\delta^2\frac{\partial w}{\partial x}\right)\left(\frac{\partial u}{\partial x}+\frac{\partial w}{\partial z}\right)$$
$$+\epsilon\delta^2\left(\frac{\partial v}{\partial x}\frac{\partial w}{\partial y}-\frac{\partial v}{\partial z}\frac{\partial u}{\partial y}\right)+\frac{\gamma}{2}\Delta\left(\frac{\partial u}{\partial z}-\delta^2\frac{\partial w}{\partial x}\right). \tag{2.7}$$

As $(\epsilon, \gamma) \to 0$, $\partial v/\partial z \to 0$ and there is no vertical shear. This limiting case is the Taylor–Proudman theorem valid for finite aspect ratio δ. Initial generation of vertical shear will be governed by the last two terms of (2.7): the tipping of the vertical component of relative vorticity into the horizontal plane and the shear zones associated with the conditions (iv) and (v). Here $\gamma \ll 1$ and the vertical shear generated by the latter mechanism is negligible except in thin boundary layers whose thickness is $O(\gamma^{\frac{1}{2}}) \ll 1$. It is important to note that within such layers the shear is locally large and $O(\gamma^{-\frac{1}{2}})$. The boundary condition (2.3b) indicates $w \sim O(\mu)$. Use of this estimate in the last two terms in (2.7) indicates that the topographically induced shear is $O(\epsilon\mu\delta^2, \gamma\mu\delta^2) + O(\delta^4)$. [The boundary condition (2.3c) with (2.6) yields a similar result with μ replaced by $\lambda\epsilon$.] Thus the magnitude of the vertical variation of the horizontal velocity over an $O(1)$ depth of fluid is

$$\max(\gamma^{\frac{1}{2}}, \epsilon\mu\delta^2, \gamma\mu\delta^2) = \gamma^{\frac{1}{2}}, \qquad (2.8)$$

by (2.4) taking $\delta^2 \ll \gamma^{\frac{1}{2}} \ll 1$.

This result suggests we study the depth-averaged flow components. Formally we separate the velocity into barotropic (z-independent) and baroclinic (z-dependent) components. For example

$$u(x,y,z,t) = \bar{u}(x,y,t) + u'(x,y,z,t), \qquad (2.9)$$

where the overbar denotes a depth average from $z = \mu b$ to $z = 1 + \lambda\epsilon p$. Note that $\overline{u'} = 0$, $\overline{\bar{u}u'} = 0$, etc. Equations for the barotropic flow components are obtained by depth averaging (2.2) with $\delta^2 = 0$. The result is

$$\epsilon \frac{d\bar{v}_i}{dt} + (1+\hat{\beta}\epsilon y)(\hat{\mathbf{z}} \times \bar{\mathbf{v}})_i = -\frac{\partial p}{\partial x_i} - \frac{1}{D}\frac{\partial}{\partial x_j}\int_{\mu b}^{1+\lambda\epsilon p} v_i' v_j' \, dz + \left[\frac{\gamma}{D}\frac{\partial v_i'}{\partial z}\right]_{\mu b}^{1+\lambda\epsilon p}, \qquad (2.10a)$$

$$\frac{dD}{dt} + D\frac{\partial v_j}{\partial x_j} = 0, \qquad (2.10b)$$

where $i(j) = 1, 2$, $D = 1 + \lambda\epsilon p - \mu b$ is the fluid depth and

$$\frac{d}{dt} \equiv \frac{\partial}{\partial t} + \bar{u}\frac{\partial}{\partial x} + \bar{v}\frac{\partial}{\partial y}.$$

The suffix notation for vector components has been introduced and the summation convention is assumed. In deriving (2.10), boundary conditions (2.3a,b) have been used.

The second term on the right-hand side of (2.10a) represents the horizontal divergence of the vertically integrated correlation of the z-dependent flow components. Its magnitude is $O(\lesssim \gamma) \ll 1$ by (2.8) and the term is dropped. The last term in (2.10a) denotes the net contribution of surface and bottom stresses and is not necessarily small. The surface stress is given by (2.3d). In principle the bottom stress may be found by solving the equations for the baroclinic flow [(2.2) with $\delta^2 = 0$ minus (2.10)] subject to conditions (2.3d,e). Such an approach is non-trivial, however, and is not pursued here. Rather the simplest closure assumption is made: that of a linear Rayleigh drag law acting anti-parallel to the velocity. Thus

$$\left[\gamma \frac{\partial \mathbf{v}'}{\partial z}\right]_{\mu b}^{1+\lambda\epsilon p} = \gamma_R(\boldsymbol{\tau} - \bar{\mathbf{v}}), \qquad (2.11)$$

where γ_R, defined in table 1 in terms of a constant coefficient of Rayleigh friction R, is $O(\gamma^{\frac{1}{2}})$.

With these simplifications, (2.10) becomes, dropping the overbar,

$$\epsilon\frac{d\mathbf{v}}{dt}+(1+\beta\epsilon y)(\hat{\mathbf{z}}\times\mathbf{v}) = -\nabla p-\frac{\gamma_R}{D}(\mathbf{v}-\boldsymbol{\tau}), \tag{2.12a}$$

$$\frac{dD}{dt}+D(\nabla\,.\,\mathbf{v}) = 0. \tag{2.12b}$$

Equations (2.12) form a closed system of three equations for u, v and D with the specification of the external stress $\boldsymbol{\tau}$ and the obstacle shape b. The external stress is discussed below. Here

$$b(x,y) = \exp\left\{-a\left[\left(\frac{x}{\sigma_x}\right)^2+\left(\frac{y}{\sigma_y}\right)^2\right]\right\}, \tag{2.13}$$

where $a = \ln 2$. Unless otherwise stated, $\sigma_x = \sigma_y = 1$, and the topography is circularly symmetric with Gaussian slopes. It falls to half its maximum value in one non-dimensional horizontal distance. A Gaussian obstacle has the advantage that it and its derivatives are continuous. Discontinuous topographies, such as disks, have large slopes, $\mu\delta \gg 1$, and would presumably excite horizontal shear layers (Stewartson 1957) and generate significant tipping of vorticity. In such cases $\epsilon\mu\delta^2$ and $\gamma\mu\delta^2$ in (2.8) would be large and the derivation of (2.12) would be invalidated. Attention is therefore restricted to obstacles of the form (2.13).

The basic set (2.12) is solved in the subsequent sections using various approximations and techniques. The steady ($\partial/\partial t \equiv 0$) form of (2.12) leads to two-dimensional elliptic equations which are solved analytically or numerically. This approach is taken in §§3–5 where the appropriate Dirichlet boundary conditions are given. In §6 the initial boundary value problem is solved numerically. The time-dependent version of (2.12) is comprised of three hyperbolic equations. For the subcritical ($\lambda\epsilon^2 < 1$) flows of interest here, two pieces of information are required on inflow and one on outflow boundaries. This information is obtained from solutions of the steady, x-independent model equations (discussed below). The details of the numerical solution and the initial conditions are provided in the next subsection.

Common to each approach (either steady or time-dependent) is the assumption of no upstream–downstream influence of the obstacle. It is assumed that a steady, x-independent solution holds far upstream ($x \to -\infty$) or downstream ($x \to +\infty$) of the topography. The alteration of the flow due to the topography is then determined. Rigorous proof of 'Long's hypothesis' in the present case is not currently available. When friction is present, any disturbance excited by the obstacle will be dissipated by the time it reaches infinity and no upstream–downstream influence is possible (see, for example, McIntyre 1972). In cases without friction (§§4–5), the free modes of the linear system are evanescent for zero frequency. Therefore no steady-state information can propagate upstream or downstream.

The flow at infinity is described by

$$\epsilon v\frac{du}{dy}-(1+\beta\epsilon y)v = -\frac{\gamma_R(u-X)}{D}, \tag{2.14a}$$

$$\epsilon v\frac{dv}{dy}+(1+\hat{\beta}\epsilon y)u = -\frac{dp}{dy}-\frac{\gamma_R v}{D}, \tag{2.14b}$$

$$\frac{d(vD)}{dy} = 0, \tag{2.14c}$$

where X is the applied zonal surface stress and Y, the meridional stress, is taken to be zero. A constant meridional mass flux is assumed of order γ_R: $vD = \gamma_R$. For a given $u(y)$, the required external stress is found from (2.14*a*) to be

$$X = u+\epsilon\frac{du}{dy}-(1+\hat{\beta}\epsilon y). \tag{2.15}$$

For example, for $u = 1$ and $\hat{\beta} = 0$, $X = 0$. Since $D \sim 1$, $v \sim \gamma_R \ll 1$, and the inflow is predominately zonal.

2.2. *Numerical model*

Numerical solutions of the time-dependent set (2.12) are obtained over a 40×40 square domain using a grid of 60×60 points (120×120 points for cases involving non-uniform inflow and 100×100 points over a 80×80 domain for the case $\gamma_R = 1{\cdot}0\times 10^{-2}$). The grid is oriented at a 45° angle relative to the zonal velocity to produce a diamond. This procedure enables upstream and downstream boundaries to be unambiguous and assures that velocity components normal to the boundary are $O(1)$ everywhere. The obstacle is placed at the centre of the domain (0, 0) and is at least 20 non-dimensional units from the boundaries. The large domain ensures that perturbations excited by the obstacle will be negligibly small upon arrival at the boundary. (A typical decay distance, ϵ/γ_R, is $\leqslant 5$ units.) The Cartesian grid is stretched in both the x' and y' directions so that $\Delta x'(\Delta y') = 0{\cdot}2$, $0{\cdot}2$, $1{\cdot}2$, $3{\cdot}0$ at $x'(y') = 0$, ± 3, ± 10, ± 20, respectively. (The primes refer to the rotated co-ordinates.) The gridpoints are staggered in space following Williams (1969) to produce an effective grid resolution of 0·1 near the obstacle.

Second-order differencing is used to express the pressure-gradient and mass-flux terms. The nonlinear advective terms are represented using the quadratic conservative scheme of Piacsek & Williams (1970); the Coriolis terms using the approach of Arakawa & Lamb (1977). A leapfrog time step is employed with the friction terms evaluated at the $\tau-1$ time level. In order to prevent the temporal separation of solutions, the $\tau-1$, τ, and $\tau+1$ time levels are averaged together every 23 time steps with weights of 0·25, 0·50, and 0·25, respectively, and the integration restarted. The start-up procedure consists of a forward time step followed by a leapfrog step, each with half the usual time interval (Miyakoda 1973). The time step is taken to be $\Delta t = 0{\cdot}05(\lambda\epsilon^2)^{-\frac{1}{2}}$.

All four sides of the domain are treated as open boundaries. On inflow, the horizontal velocity is specified; on outflow, the normal velocity component. In addition to these physical conditions, computational boundary conditions are provided by linear extrapolation. In order to minimize the spurious reflexion of transients at the boundaries, the approach of Orlanski (1976) is adopted in modified form (Bannon 1979).

The initial free-surface height field is that obtained from the solution of the zonally symmetric model equations, (2.14). The solution is found using a fourth-order Runge–Kutta technique. It also provides the Dirichlet boundary conditions. The velocity field is then determined by satisfying the balance condition of mass flux continuity over the variable bottom topography. This procedure results in the largest velocities being located over the obstacle (for $\mu > 0$). This initialization and the presence of viscosity preclude the formation of a vortex pair as discussed by Johnson (1978*a*).

For each experiment discussed in § 6, the equations were integrated forward in time for 8 frictional spindown times ($\tau_s = \epsilon/\gamma_R$) by which time a steady state had been achieved. The results displayed here are based on the fields calculated at the end of the integration. The numerical technique was verified by reproducing the steady-state calculations of § 3 for the case $\epsilon = 0$ and of § 4 for the Oseen approximation to quasi-geostrophic theory for $\mu = 1{\cdot}305\epsilon$ and $\gamma_R = 0{\cdot}2\epsilon$.

In the course of some of the numerical integrations, a weak two-delta grid oscillation develops in the velocity components where the fields are small. This oscillation has zero phase speed and represents a spurious spatial mode excited by the finite-difference scheme for the advective accelerations. It is believed that this computational noise does not seriously affect the solutions because (1) the effect of the oscillation is automatically removed from many of the terms in the equations by the averaging associated with the differencing scheme, (2) the height field H is smooth, (3) the computation is stable, and (4) tests with a lateral viscosity with $\gamma = 0{\cdot}04\,\gamma_R$ produced results similar to the laterally inviscid calculation but without the oscillation. The numerical results presented in § 6 are based on the unsmoothed fields computed with no lateral viscosity.

3. Steady linear solution with friction

In order to ascertain the effects of the nonlinear inertial terms, solutions of the linearized model equations are now presented which may be compared with the subsequent nonlinear calculations. In the limit of $\epsilon \to 0$ with $\beta \sim O(1)$ and $\lambda \sim O(1)$, (2.12*a, b*) become, with no external stress,

$$-v = -\frac{\partial p}{\partial x} - \frac{\gamma_R u}{(1-\mu b)}, \tag{3.1a}$$

$$u = -\frac{\partial p}{\partial y} - \frac{\gamma_R v}{(1-\mu b)}, \tag{3.1b}$$

$$-\mu\left(u\frac{\partial b}{\partial x} + v\frac{\partial b}{\partial y}\right) + (1-\mu b)\left(\frac{\partial u}{\partial x} + \frac{\partial v}{\partial y}\right) = 0. \tag{3.1c}$$

It is noted that the presence of the free surface has no effect. Solving (3.1*a*) and (3.1*b*) for u and v in terms of p and substituting into (3.1*c*) yields an elliptic equation for p:

$$\nabla^2 p = \frac{1}{\gamma_R}J(p,e) + \frac{e}{\gamma_R}J(p,c) - \left(\frac{\partial c}{\partial x}\frac{\partial p}{\partial x} + \frac{\partial c}{\partial y}\frac{\partial p}{\partial y}\right), \tag{3.2}$$

where

$$e = (1-\mu b), \quad c = \ln\left[e^2/(\gamma_R^2 + e^2)\right],$$

and $J(S,T) = -S_y T_x + S_x T_y$ is the Jacobian operator.

Far upstream of the obstacle at (0, 0), the flow satisfies (2.14) with $\epsilon = 0$. Letting $v = v_0 =$ constant, the solution is

$$u_\infty = v_0/\gamma_R, \quad v_\infty = v_0, \quad p_\infty = p_{00} - \gamma_R v_0 y - v_0 y/\gamma_R, \tag{3.3a,b,c}$$

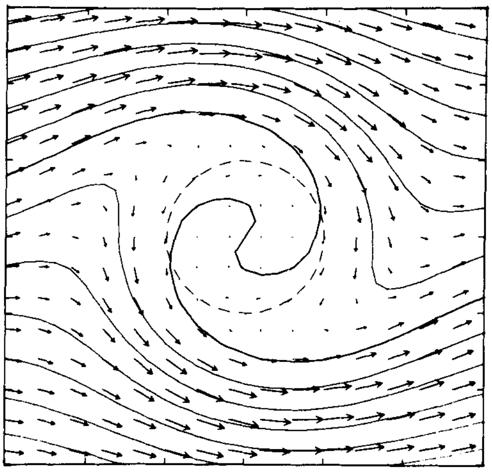

FIGURE 2. Velocity vector field and pressure contours for linear viscous flow with $\mu = 0{\cdot}522$ and $\gamma_R = 2\times10^{-2}$. C.I. $= 0{\cdot}4$. MV $= 1{\cdot}52$. In this and all subsequent figures, the dashed circle of unit radius is the contour of the bottom topography at half its maximum value μ; C.I. is the contour interval of the non-dimensional pressure field; MV denotes the speed of the largest velocity vector; the heavy contour line refers to the pressure field at $(x = -\infty, y = 0)$.

where p_{00} is an arbitrary constant. The subscript ∞ denotes the x-independent flow solution far from the obstacle. With $v_0 = \gamma_R$, $u_\infty = 1$.

Numerical solutions of (3.2) are found on a 20×20 square domain using a fourth-order finite-difference scheme with a uniform mesh $\Delta = 0{\cdot}2$. On all four boundaries $p = p_\infty$. Because the spectral radius of convergence of the appropriate iteration matrix (see, for example, Smith 1975) is greater than unity, iterative methods (e.g. successive over-relaxation) could not be utilized. Here the solution is obtained by direct inversion of the matrix equation.

Figure 2 displays the result obtained for the case of uniform inflow $(u_\infty = 1, v_\infty = \gamma_R)$ for $\gamma_R = 2{\cdot}0\times10^{-2}$ with $\mu = 0{\cdot}522$. (The particular choice of μ used here will be made apparent in the next section.) The upstream flow is deflected around the obstacle with a stagnant region (Taylor column) over the obstacle. For larger γ_R (not shown), the deflexion of the incident flow is less. The essence of the physics is contained in the first two terms in (3.2)

$$\nabla^2 p \sim -(\mu/\gamma_R)J(p,b), \tag{3.4}$$

which states that the frictional dissipation of vorticity due to Ekman pumping (left-hand side) is balanced by orographic vortex stretching (right-hand side). A viscous Taylor column $(J(p,b) \simeq 0)$ will form provided $\mu \gg \gamma_R$.

This result is in agreement with the analysis of Jacobs (1964) who solved the steady, three-dimensional linear problem. Jacobs's analysis predicts that the flow about the obstacle reduces to that of two-dimensional potential theory in the limit $\gamma \rightarrow 0$. Such a flow possesses upstream–downstream and left–right symmetry. The deviations from this solution displayed in figure 2 are presumably caused by γ_R being finite. The topographic enhancement of the friction $[\gamma_R/(1-\mu b)$ *vs.* γ_R in (3.1*a*) and (3.1*b*)] is not responsible for the deviations.

γ_R	$B(1)$	$B(2)$	$B(3)$	$\hat{C}_E$	$\hat{C}_T$	$(\hat{C}_E+\hat{C}_T)$
$2{\cdot}0\times10^{-3}$	1·00	1·03	0·65	0·53	1·03	1·56
$2{\cdot}0\times10^{-2}$	1·06	0·75	0·36	0·75	0·56	1·31
$2{\cdot}0\times10^{-1}$	0·59	0·27	0·12	0·96	0·14	1·10

TABLE 2. Blocking efficiency and drag coefficients for linear viscous flow with $\mu = 0{\cdot}522$; $A = 0$.

It is convenient at this time to introduce two non-dimensional ratios which measure the blocking efficiency of the topography, $B(y)$, and the asymmetry of the flow around the obstacle, $A(y)$. Let

$$B(y) = 1-\frac{F^+(0,y)+F^-(0,y)}{F^+(-\infty,y)+F^-(-\infty,y)}, \tag{3.5a}$$

$$A(y) = \frac{F^+(0,y)/F^+(-\infty,y)}{F^-(0,y)/F^-(-\infty,y)}-1, \tag{3.5b}$$

where

$$F^{\pm}(x,y) = \pm\int_0^{\pm y} u(x,\eta)\,D(x,\eta)\,d\eta$$

is the zonal mass flux. For a Taylor column of radius y_c, $B(y\leqslant y_c) = 1$. Note that $B(\infty) = 0$ and that $A(y) = 0$ for symmetric flow. For linear viscous flows, $A(y) = 0$. The left–right symmetry of the solutions is also reflected in the fact that the contour line of the pressure field (streamline) originating at $(x = -\infty, y = 0)$ crosses the y axis at $y = 0$. Table 2 gives the blocking efficiencies for various values of γ_R with $\mu = 0{\cdot}522$. A value of $B > 1$ indicates the presence of a return flow $(u < 0)$ over the obstacle.

It is also of interest to determine the total drag exerted on the flow due to the presence of the obstacle. Define a frictional or Ekman drag and a topographic drag by:

$$\frac{F_E}{\rho_0 U_0\, fL^3} = C_E = \delta\gamma_R\iint u\,dxdy, \tag{3.6a}$$

$$\frac{F_T}{\rho_0 U_0\, fL^3} = C_T = \delta\mu\iint p\frac{\partial b}{\partial x}dxdy, \tag{3.6b}$$

respectively. Since $\partial b/\partial x$ is odd in x and even in y, $C_T = 0$ if p is even in x or odd in y. It is convenient to normalize these drag coefficients by that drag present in the absence of an obstacle:

$$C_N = \delta\gamma_R\iint u_\infty(y)\,dxdy. \tag{3.7}$$

Thus define

$$\hat{C}_E = C_E/C_N \quad\text{and}\quad \hat{C}_T = C_T/C_N.$$

Table 2 presents the results. The integrals are taken over the domain of figure 2. Note the increase (decrease) in $\hat{C}_T(\hat{C}_E)$ with decreasing γ_R. In each case, however,

$$\hat{C}_T+\hat{C}_E > 1,$$

indicating that the total drag is greater than that in the absence of an obstacle.

μ	ζ_∞	$A(1)$	$A(2)$	$A(3)$
$\frac{1}{2}\mu_c$	0	0·77	1·22	1·21
μ_c	0	2·49	6·31	6·17
$2\mu_c$	0	−20·51	−5·86	−5·92
$\frac{1}{2}\mu_c$	$-\frac{1}{4}$	0·82	1·64	2·22
$\frac{1}{2}\mu_c$	$+\frac{1}{4}$	0·75	1·16	1·21

TABLE 3. Asymmetry function for inviscid quasi-geostrophic flow. $B = \hat{C}_T = 0$.

4. Quasi-geostrophic theory

Here inertial effects are introduced using the quasi-geostrophic approximation. Assuming $(\gamma_R, \mu) \lesssim \epsilon \ll 1$ and $(\lambda, \hat{\beta}) \lesssim 1$, the dependent variables may be expressed in terms of a perturbation series expansion in ϵ. For example

$$p = p_0 + \epsilon p_1 + \epsilon^2 p_2 + \ldots + \epsilon^n p_n + \ldots. \tag{4.1}$$

Substitution of such series into (2.12) and retention of only the $O(1)$ term yields the result that the flow is geostrophic and non-divergent. The $O(\epsilon)$ equations may be combined in a straightforward manner to yield

$$\frac{d}{dt_0}\left[\nabla^2 p_0 - \lambda p_0 + \frac{\mu b}{\epsilon} + \hat{\beta} y\right] = -\frac{\gamma_R}{\epsilon}\nabla^2 p_0, \tag{4.2}$$

where

$$\frac{d}{dt_0} = \frac{\partial}{\partial t} + u_0\frac{\partial}{\partial x} + v_0\frac{\partial}{\partial y}.$$

The result (4.2) is consistent with the usual quasi-geostrophic theory (e.g. Johnson 1978*b*; Stevenson & Janowitz 1977) provided $\gamma_R = \gamma^{\frac{1}{2}}$. The degeneracy of the zeroth-order flow can now be removed through consideration of (i) time dependence, (ii) topographic effects, and/or (iii) friction. In the steady state, (4.2) may be written

$$J\left[p_0, \nabla^2 p_0 - \lambda p_0 + \frac{\mu b}{\epsilon} + \hat{\beta} y\right] = -\frac{\gamma_R}{\epsilon}\nabla^2 p_0. \tag{4.3}$$

Since $J(p_0, p_0) = 0$, quasi-geostrophic theory indicates no free surface effects in the steady state (Johnson 1978*b*).

For $\gamma_R = 0$, (4.3) states that the quantity $[\nabla^2 p_0 + \mu b/\epsilon + \hat{\beta} y]$ is conserved along streamlines. Therefore, knowledge of the flow upstream enables the flow to be determined everywhere provided no closed streamlines exist. Setting $\hat{\beta} = 0$ and assuming a zonal inflow at $x = -\infty$ of the form $u = u_\infty - \zeta_\infty y$, the solution is (Cottrell 1970; Huppert 1975)

$$p_0 = -u_\infty y + \tfrac{1}{2}\zeta_\infty y^2 + \frac{\mu}{2a\epsilon}\sum_{n=1}^{\infty}\frac{(-1)^n}{2n}\frac{(ar^2)^n}{n!}, \tag{4.4}$$

where $r^2 = x^2 + y^2$ and $a = \ln 2$. For $u_\infty = 1$ and $\zeta_\infty = 0$, Huppert (1975) showed that the condition for the formation of a closed streamline (Taylor column) over a Gaussian mountain is that $\mu > \mu_c = 2{\cdot}61\epsilon$. The column grows from the point $(r, \theta) = (1{\cdot}35, -\frac{1}{2}\pi)$. [Differences in numerical constants used here and in Huppert (1975) arise from different scaling.]

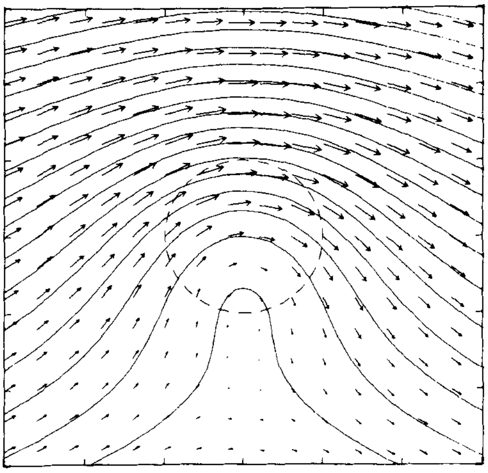

FIGURE 3. Inviscid quasi-geostrophic flow for $u_\infty = 1$, $\zeta_\infty = 0$, and $\mu = \mu_c$. C.I. = 0·4. MV = 1·99.

Table 3 summarizes the results. Figure 3 plots the solution (4.4) with $u_\infty = 1$ and $\zeta_\infty = 0$ for $\mu = \mu_c$. The solutions possess upstream–downstream symmetry but have considerable left–right asymmetry. The left–right asymmetry is also reflected in the fact that the streamline originating at $(x = -\infty, y = 0)$ crosses the y axis at $y = +\infty$. This feature is a consequence of the fact that the last term in (4.4) represents a monopole of vorticity with circulation $\Gamma = (\mu\pi/\epsilon a)(e^{-ar^2} - 1)$ which is non-zero at infinity. In contrast linear viscous flow (figure 2) exhibits a dipole-type field. The asymmetry increases with increasing obstacle height. Upon the formation of a Taylor column to the right of the obstacle centre $(\mu > \mu_c)$ with the associated return flow $(u < 0)$, $A(y)$ becomes negative. Because of the symmetry of the solutions (4.4), $B(y) \equiv 0$, $\hat{C}_E = 1$ and $C_T \equiv 0$. Thus quasi-geostrophic theory calculates no blocking of the flow. This shortcoming is a consequence of the non-divergent character of the flow. The obstacle acts only on the rotational flow component through the mechanism of vortex stretching. The divergent flow component is unaffected. The lack of a topographic drag is a consequence of d'Alembert's paradox: in the absence of wave motion, steady inviscid flow can produce no drag. Table 3 also gives $A(y)$ for $u_\infty = 1$, $\mu = \frac{1}{2}\mu_c$ and $\zeta_\infty = \pm\frac{1}{4}$. As noted by Cottrell (1970), a background flow with anticyclonic shear provides an environment better suited for the formation of Taylor columns by increasing the flow asymmetry.

Frictional effects were taken into account by Vaziri & Boyer (1971) who treated (4.2) as an initial, boundary-value problem on an f-plane. Their results show that the incorporation of friction destroys the upstream–downstream symmetry present in the inviscid results (see figure 3). The reason for the asymmetry is revealed most easily by applying the Oseen approximation to (4.3). This approach has been used previously by Huppert & Stern (1974) for ridge-like obstacles on the f-plane and by Stevenson & Janowitz (1977) for point sources on the β-plane. With such an approximation, (4.3) becomes

$$\nabla^2 p_0 = -\beta y - \frac{\mu b}{\epsilon} - \frac{\gamma_R}{\epsilon}\int_{-\infty}^{x} \nabla^2 p_0\, dx. \tag{4.5}$$

This elliptic equation with $\beta = 0$ was solved numerically on a 20×20 domain with 100×100 gridpoints using the technique of successive-over-relaxation with $p_0 = -y$ on the boundaries (i.e. uniform inflow $u_\infty = +1$). The frictional term was treated as a small perturbation ($\gamma_R/\epsilon = 0{\cdot}2$) of a known function based on a previous iterative solution. Initially $\nabla^2 p_0 = -\mu b/\epsilon$. The technique was convergent and the solution for $\mu = \frac{1}{2}\mu_c$ and $\gamma_R/\epsilon = 0{\cdot}2$ is similar to figure 7 (*c*) and is not shown. As with the previous quasi-geostrophic results, $B(y) = 0$. Here $A(y) = 0{\cdot}47$, $0{\cdot}68$, $0{\cdot}64$ for $y = 1, 2, 3$, and the reference streamline exhibits a finite deflexion to the left upon crossing the y axis. Thus friction reduces the left–right asymmetry, implying that inertial Taylor columns are less likely to form in the presence of friction. The upstream–downstream asymmetry produces a topographic drag: $\hat{C}_T = 0{\cdot}13$, $\hat{C}_E = 1{\cdot}00$.

5. Steady inviscid flow

Here we ascertain the effects of finite Rossby number ϵ and of the presence of a free surface on the formation of a Taylor column. The method of solution follows that of Charney (1955). The three equations of the set (2.12) may be manipulated to form vorticity and energy equations. With $\boldsymbol{\tau} = \gamma_R = 0$, the steady-state equations plus continuity are

$$\mathbf{v}.\nabla\left[\frac{1+\beta\epsilon y+\epsilon\zeta}{D}\right] = 0, \tag{5.1a}$$

$$\mathbf{v}.\nabla\left[\frac{u^2+v^2}{2}+\frac{1}{\lambda\epsilon^2}+\frac{p}{\epsilon}\right] = 0, \tag{5.1b}$$

$$\nabla.(\mathbf{v}D) = 0, \tag{5.1c}$$

where $\zeta = \partial v/\partial x - \partial u/\partial y$ is the relative vorticity. Introduction of a mass flux stream function ψ:

$$uD = -\partial\psi/\partial y, \quad vD = +\partial\psi/\partial x, \tag{5.2a,b}$$

satisfies (5.1*c*) identically. Equations (5.1*a*) and (5.1*b*) then become

$$\frac{1}{D}J\left[\psi, \frac{1+\beta\epsilon y+\epsilon\zeta}{D}\right] = 0, \tag{5.3a}$$

$$\frac{1}{D}J\left[\psi, \frac{u^2+v^2}{2}+\frac{1}{\lambda\epsilon^2}+\frac{p}{\epsilon}\right] = 0. \tag{5.3b}$$

Thus, provided there are no closed streamlines, we have

$$\frac{1+\beta\epsilon y+\epsilon\zeta}{D} = F(\psi), \tag{5.4a}$$

$$\frac{u^2+v^2}{2}+\frac{1}{\lambda\epsilon^2}+\frac{p}{\epsilon} = G(\psi), \tag{5.4b}$$

where F and G are functions to be determined and

$$\zeta = \frac{\partial}{\partial x}\left(\frac{1}{D}\frac{\partial\psi}{\partial x}\right)+\frac{\partial}{\partial y}\left(\frac{1}{D}\frac{\partial\psi}{\partial y}\right). \tag{5.5}$$

Hereafter we restrict attention to cases with $\beta = 0$.

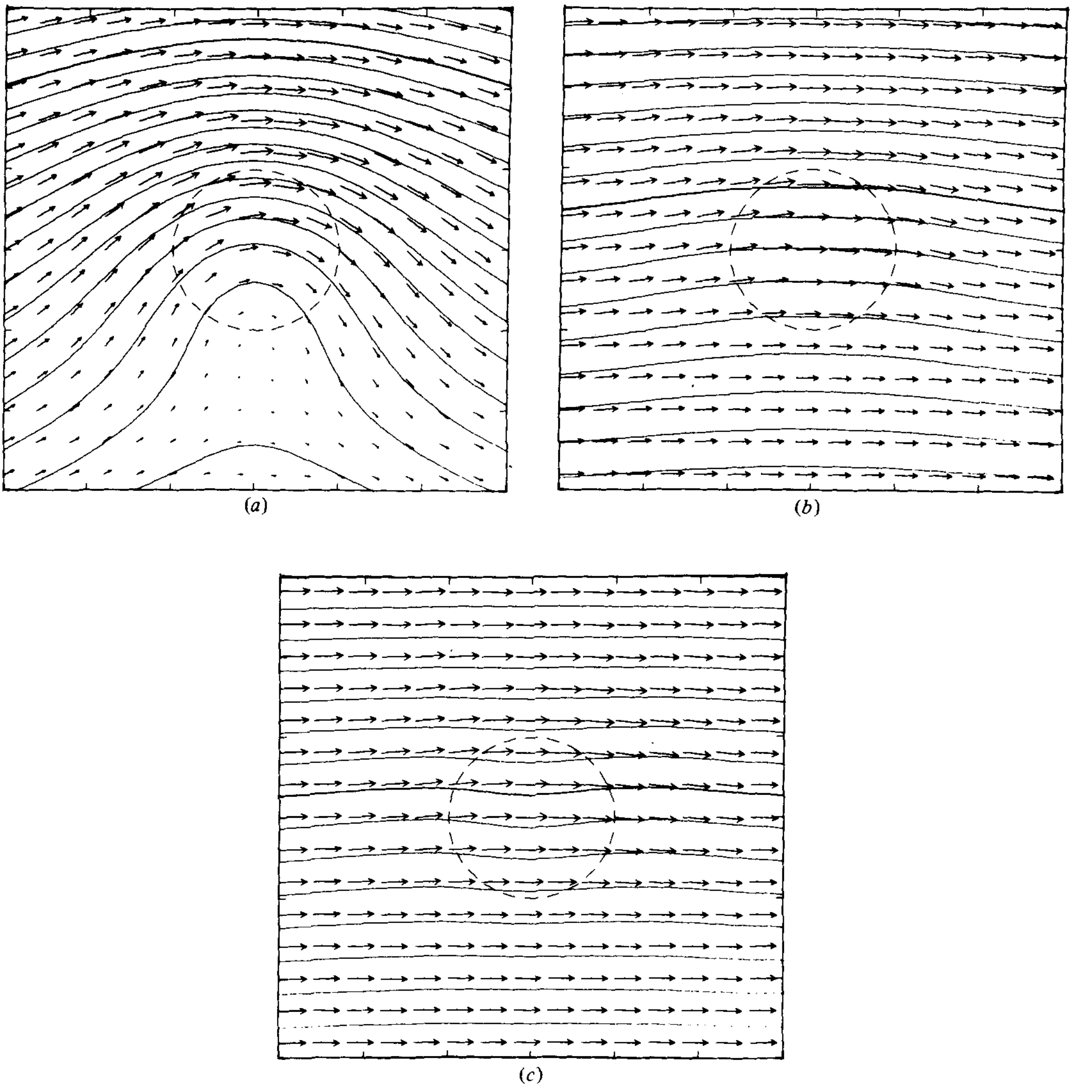

(*a*)

(*b*)

(*c*)

FIGURE 4. Nonlinear inviscid flow subject to a rigid lid for $\mu = 0{\cdot}261$. C.I. $= 0{\cdot}4$. (*a*) $\epsilon = 0{\cdot}1$, MV $= 2{\cdot}07$. (*b*) $\epsilon = 0{\cdot}5$, MV $= 1{\cdot}29$. (*c*) $\epsilon = 1{\cdot}0$, MV $= 1{\cdot}20$.

5.1. *Effect of finite Rossby number*

In the case of a rigid lid ($\lambda = 0$), $D = 1-\mu b$ and the set (5.4) is decoupled. For uniform upstream inflow at $x = -\infty$,

$$u_\infty = 1, \quad v_\infty = 0, \quad D_\infty = 1, \quad \psi_\infty = -y, \quad p_\infty = -y. \tag{5.6}$$

Hence $F(\psi) = F(\psi_\infty) = 1$ and $G(\psi) = G(\psi_\infty) = \psi/\epsilon + \frac{1}{2} + 1/\lambda\epsilon^2$. As noted by Charney (1955) $\epsilon dG/d\psi = F$. Thus (5.4*a*) becomes an elliptic equation for ψ:

$$\nabla^2\psi = \frac{\partial \ln D}{\partial x}\frac{\partial \psi}{\partial x} + \frac{\partial \ln D}{\partial y}\frac{\partial \psi}{\partial y} - \frac{\mu b D}{\epsilon}. \tag{5.7}$$

ϵ	$A(1)$	$A(2)$	$A(3)$
0·1	1·96	4·78	4·93
0·5	0·22	0·33	0·33
1·0	0·10	0·15	0·15

TABLE 4. Asymmetry function for inviscid flow with finite ϵ and $\lambda = 0$ for $\mu = 0{\cdot}261$; $\hat{C}_T = 0$.

Johnson (1978*a*) solved (5.7) analytically for a right circular cylinder. Here it is solved numerically for the obstacle (2.13) by S.O.R. over a 20×20 domain with $\psi = \psi_\infty$ on the boundaries. The velocity field and pressure pattern may then be obtained from (5.2) and (5.4*b*), respectively.

Figure 4 displays the resulting solutions with $\mu = 0{\cdot}261$ for $\epsilon = 0{\cdot}1,\ 0{\cdot}5,\ 1{\cdot}0$. Comparison for figures 4(*a*) and 3 clearly shows that a finite ϵ decreases the asymmetry of the flow (see also tables 3 and 4) and increases the strength of the topography required to produce a Taylor column. For $\epsilon = 0{\cdot}1$, a Taylor column ($u < 0$) forms for $\mu \gtrsim 1{\cdot}10\mu_c$. Note that by the symmetry of the pressure pattern, $C_T = 0$. In contrast with the quasi-geostrophic result, the reference pressure line crosses the y axis at finite y. Its leftward displacement decreases with increasing ϵ, suggesting that its finite value is a physical result and not a consequence of the limited domain.

As ϵ increases, the single high pressure perturbation present in figure 4(*a*) splits into two cells up- and downstream of the obstacle centre with a central trough (figure 4*c*). [For still larger ϵ, this trough intensifies and becomes the dominant flow feature. The solution for $\epsilon = 10$ (not shown) is qualitatively similar to the mirror image (i.e. reflexion about the x axis) of figure 4(*a*).] This behaviour in the pressure field was also noted by Buzzi & Tibaldi (1977) who calculated higher-order ageostrophic effects using a perturbation expansion in ϵ. The pressure trough is not associated with a cyclonic vortex† since the relative vorticity $\zeta = -\mu b/\epsilon$. For fixed μ, as $\epsilon \rightarrow \infty$, $\zeta \rightarrow 0$, and $A(y) \rightarrow 0$ (see table 4). For flow over the obstacle, continuity requires an increase in flow speed, and thus, by Bernoulli's theorem, (5.4*b*), a pressure drop develops over the obstacle for large ϵ. For small ϵ, the flow intensification is accomplished by a left–right pressure gradient over the obstacle.

A remarkable feature of the solutions to (5.7) is that the blocking efficiency is independent of ϵ: $B(y) = 0{\cdot}10,\ 0{\cdot}05,\ 0{\cdot}02$ for $y = 1, 2, 3$, respectively. This result implies that $B(y)$ is dependent only on the magnitude and shape of the obstacle. The general solution to (5.7) (Johnson 1978*a*) can be written as the sum of the solution of the homogeneous equation subject to inhomogeneous boundary conditions and of the solution of the inhomogeneous equation with homogeneous boundary conditions. Only the former solution contributes to $B(y)$. The latter corresponds to a topographically bound vortex (e.g. Merkine & Kalnay-Rivas 1977) which is independent of the upstream flow conditions. It contributes to the left–right asymmetry of the flow but not to the blocking efficiency.

It is convenient at this point to discuss the effects of a topographic depression, $\mu < 0$, rather than an elevation, $\mu > 0$. Quasi-geostrophic theory indicates that a

---

† The presence of cyclonic vorticity in the inertial solution of Buzzi & Tibaldi (1977) presumably arises because of the inclusion of a finite number of terms in the series representation.

depression produces a cyclonic eddy whose magnitude is the same (for equal $|\mu|$) as the anticyclonic response to an elevation. Finite ϵ solutions with $\mu < 0$ also displayed cyclonic disturbances. Though the topographically induced vorticity, $\zeta = -\mu b/\epsilon$, has the same magnitude for $\mu = \pm\mu_0$, continuity constraints require larger streamline curvature, $\nabla^2\psi \sim -\mu b(1-\mu b)/\epsilon$, for $\mu = -\mu_0$. This effect produces a more asymmetric flow†: for $\epsilon = 0{\cdot}1$ and $\mu = -0{\cdot}261$, $A'(y) = 1/(A(y)+1)-1 = 3{\cdot}02$, $8{\cdot}26$, $7{\cdot}77$ for $y = 1, 2, 3$, respectively, and closed streamlines are present in the solution (not shown). These results should be compared with table 4. In addition, a depression causes the coefficients of the homogeneous form of (5.7) to be reversed in sign and reduced in magnitude so that $B(y) = -0{\cdot}09$, $-0{\cdot}04$, $-0{\cdot}02$ for $y = 1, 2, 3$, respectively. Negative blocking indicates that the zonal mass flux is greater over the obstacle than it is far upstream. This intensification arises because of continuity requirements. As noted previously, $B(y)$ is independent of ϵ and identical to the non-rotating case.

5.2. *Effect of free surface*

As noted by Johnson (1978*b*), quasi-geostrophic theory indicates that the presence of a free surface has no effect on steady-state flow. Here the ageostrophic free-surface effects are deduced. For uniform inflow at $x = -\infty$,

$$\left.\begin{aligned} u_\infty = 1, \quad v_\infty = 0, \quad p_\infty = -y, \\ D_\infty = 1+\lambda\epsilon p_\infty, \quad \psi_\infty = p_\infty + \tfrac{1}{2}\lambda\epsilon p_\infty^2. \end{aligned}\right\} \tag{5.8}$$

The last equation may be solved for p:

$$p_\infty = \frac{-1+(1+2\lambda\epsilon\psi_\infty)^{\frac{1}{2}}}{\lambda\epsilon}, \tag{5.9}$$

where the positive root is taken to assure that $p_\infty \rightarrow \psi_\infty$ as $\lambda \rightarrow 0$. Thus

$$G(\psi) = G(\psi_\infty) = \tfrac{1}{2} + \frac{1}{\lambda\epsilon^2}(1+2\lambda\epsilon\psi)^{\frac{1}{2}} \quad \text{and} \quad F(\psi) = +(1+2\lambda\epsilon\psi)^{-\frac{1}{2}}.$$

Substitution into (5.4) yields

$$\nabla^2\psi = +\frac{\partial \ln D}{\partial x}\frac{\partial\psi}{\partial x} + \frac{\partial \ln D}{\partial y}\frac{\partial\psi}{\partial y} + \frac{D}{\epsilon}[D(1+2\lambda\epsilon\psi)^{-\frac{1}{2}} - 1], \tag{5.10a}$$

$$p = \frac{\epsilon}{2}[1-(u^2+v^2)] + \frac{1}{\lambda\epsilon}[(1+2\lambda\epsilon\psi)^{\frac{1}{2}} - 1]. \tag{5.10b}$$

This set is coupled because $D = D(p)$ here. A solution is obtained numerically as in § 5.1, but free surface effects are included after each approximate solution is found by updating the right-hand side of (5.10*a*) iteratively. The technique is convergent after 750 iterations.

Plots of the solutions for $\mu = \mu_c = 0{\cdot}261$ are similar to those in figure 4 (*a*) and are not displayed. As the inertio-gravity waves of zero frequency are evanescent, no waves are present in the lee of the obstacle. The pressure field is an even function in x so $C_T \equiv 0$. Table 5 summarizes the results. The presence of a free surface decreases the blocking

---

† Redefinition of the asymmetry function for $\mu < 0$ facilitates direct comparison with results for $\mu > 0$.

λ	$B(1)$	$B(2)$	$B(3)$	$A(1)$	$A(2)$	$A(3)$
10^{-2}	0·10	0·04	0·02	1·95	4·75	4·89
10^{-1}	0·08	0·03	0·01	1·90	4·48	4·58

TABLE 5. Blocking and asymmetry functions for inviscid flow with finite λ for $\epsilon = 10^{-1}$ and $\mu = 0{\cdot}261$; $C_T = 0$.

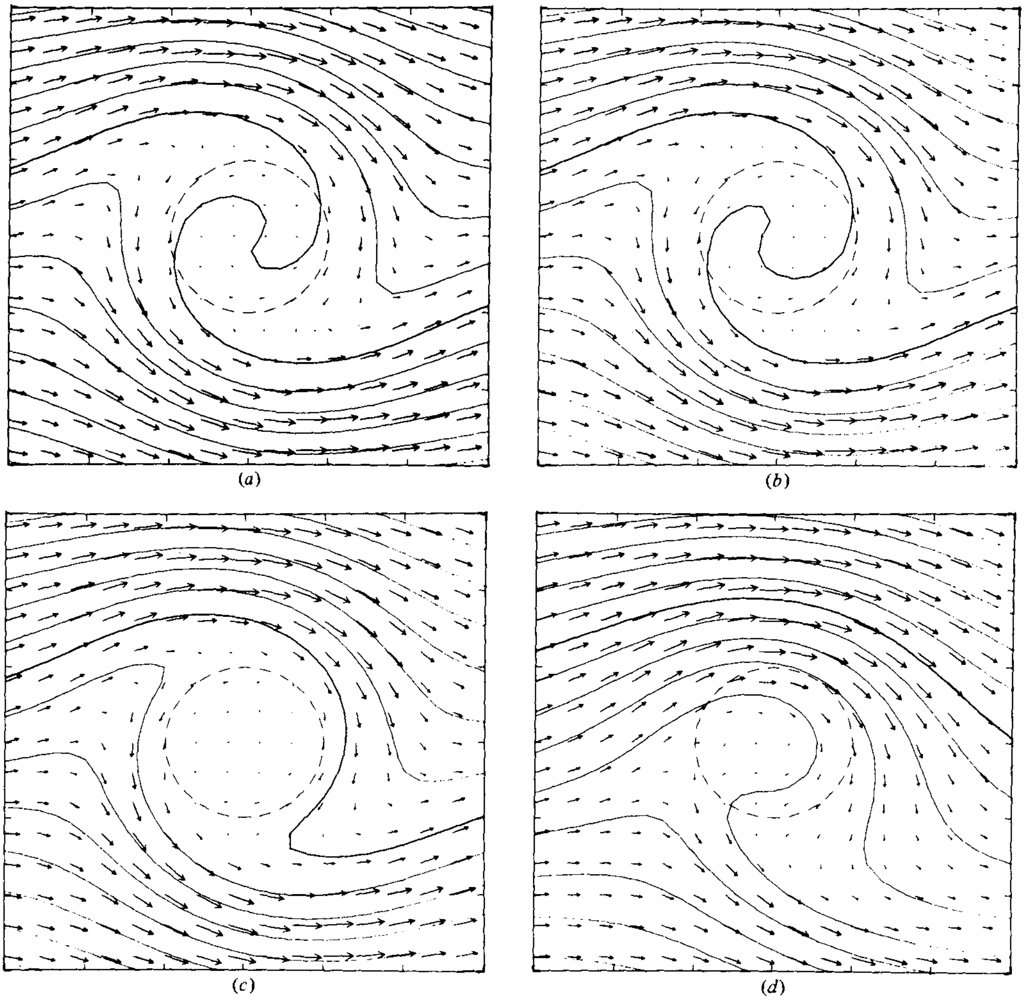

FIGURE 5. Numerical solutions as a function of ϵ for $\gamma_R = 2{\cdot}0 \times 10^{-2}$, $\lambda = 10^{-1}$, and $\mu = 0{\cdot}522$. C.I. = 0·4. (*a*) $\epsilon = 10^{-4}$, MV = 1·51. (*b*) $\epsilon = 10^{-3}$, MV = 1·52. (*c*) $\epsilon = 10^{-2}$, MV = 1·53. (*d*) $\epsilon = 10^{-1}$, MV = 1·65.

action of the obstacle and reduces the flow asymmetry. The anticyclonic vortex generated by the orographic vortex compression ($\mu > 0$) has associated with it a positive free surface deflexion. This elevation of the free surface partially negates the squashing of vortex tubes by the orography. Thus the magnitude of the topographic vortex generated by the last term in (5.10*a*) is reduced and consequently so too is the

ϵ	$B(1)$	$B(2)$	$B(3)$	$A(1)$	$A(2)$	$A(3)$	$\hat{C}_E$	$\hat{C}_T$
10^{-4}	1·06	0·77	0·37	−0·00	0·01	0·00	0·74	0·57
10^{-3}	1·06	0·77	0·37	−0·01	0·06	0·02	0·74	0·57
10^{-2}	1·06	0·76	0·36	−0·10	0·84	0·19	0·74	0·57
10^{-1}	0·90	0·56	0·28	−3·87	24·72	2·06	0·78	0·65

TABLE 6. Blocking and asymmetry functions and drag coefficients as a function of ϵ for $\gamma_R = 2{\cdot}0\times 10^{-2}$, $\lambda = 10^{-1}$ and $\mu = 0{\cdot}522$.

flow asymmetry. Furthermore the positive free-surface deflexion diminishes the continuity effects represented by the first two terms on the right-hand side of (5.10*a*). Thus the blocking of the flow is reduced. In the limit as $\epsilon \rightarrow 0$ with $\lambda\epsilon \sim O(1)$,

$$(A(y), B(y)) \rightarrow 0,$$

and the flow is unaffected by the obstacle except for a free surface deflexion

$$p = p_\infty + \mu b/\lambda\epsilon$$

which assures mass continuity.

It should be noted that these results hold for rotating flow where $\epsilon \ll 1$. As figure 4(*c*) indicates, negative free surface deflexion is present over elevations for $\epsilon \gtrsim 1$. In such cases the free surface provides a positive feedback.

6. Results of numerical integrations of initial boundary value problem

The first series of experiments is designed to display the effect of variations in the Rossby number ϵ (e.g. variation in the strength of the inflow). In each experiment, $\gamma_R = 2{\cdot}0\times 10^{-2}, \lambda = 10^{-1}, \mu = 0{\cdot}522, \beta = 0$, and the zonal flow at $x = -\infty$ is $u_\infty(y) = 1$. The computed fields as a function of ϵ are displayed in figure 5 and the relevant flow quantities in table 6. For $\epsilon = 10^{-4}$ the solution agrees with the linear analysis of §3 (see figure 2 and table 2). For increasing ϵ, the blocking efficiency decreases, the asymmetry increases, and the total drag increases. Note that the strongly inertial solution of figure 5(*d*) ($\epsilon/\gamma_R = 5$) is strikingly different from the inviscid ($\epsilon/\gamma_R = \infty$) result of figure 4(*a*). (As the height of the obstacle is different in the two figures, only qualitative comparison may be made.) The former possesses large upstream–downstream asymmetry which is lacking in the latter. Owing to the presence of friction, the region of stagnant fluid is rotated ~ 90° in a clockwise direction relative to its inviscid location directly to the right of centre.

The effects of changes in the strength of the friction coefficient γ_R are shown in figure 6 and table 7. In each experiment $\epsilon = 10^{-1}$, $\lambda = 10^{-1}$, $\beta = 0$, $\mu = 0{\cdot}522$, and $u_\infty(y) = 1$. For increasing γ_R, the blocking efficiency of the obstacle, the flow asymmetry, and the total drag decrease except for $\gamma_R = 10^{-2}$ whose blocking efficiency is less than that for $\gamma_R = 2{\cdot}0\times 10^{-2}$. This suggests that a threshold in $B(y)$ has been superseded. A further decrease in γ_R would then produce a further reduction in blocking efficiency until the inviscid results of table 5 would be attained with the concomitant small $B(y)$. The counter-clockwise shift of the centre of the anticyclonic cell from figure 6(*b*) to 6(*a*) also suggests this trend toward the inviscid results with the stagnant region located directly to the right of the obstacle's centre.

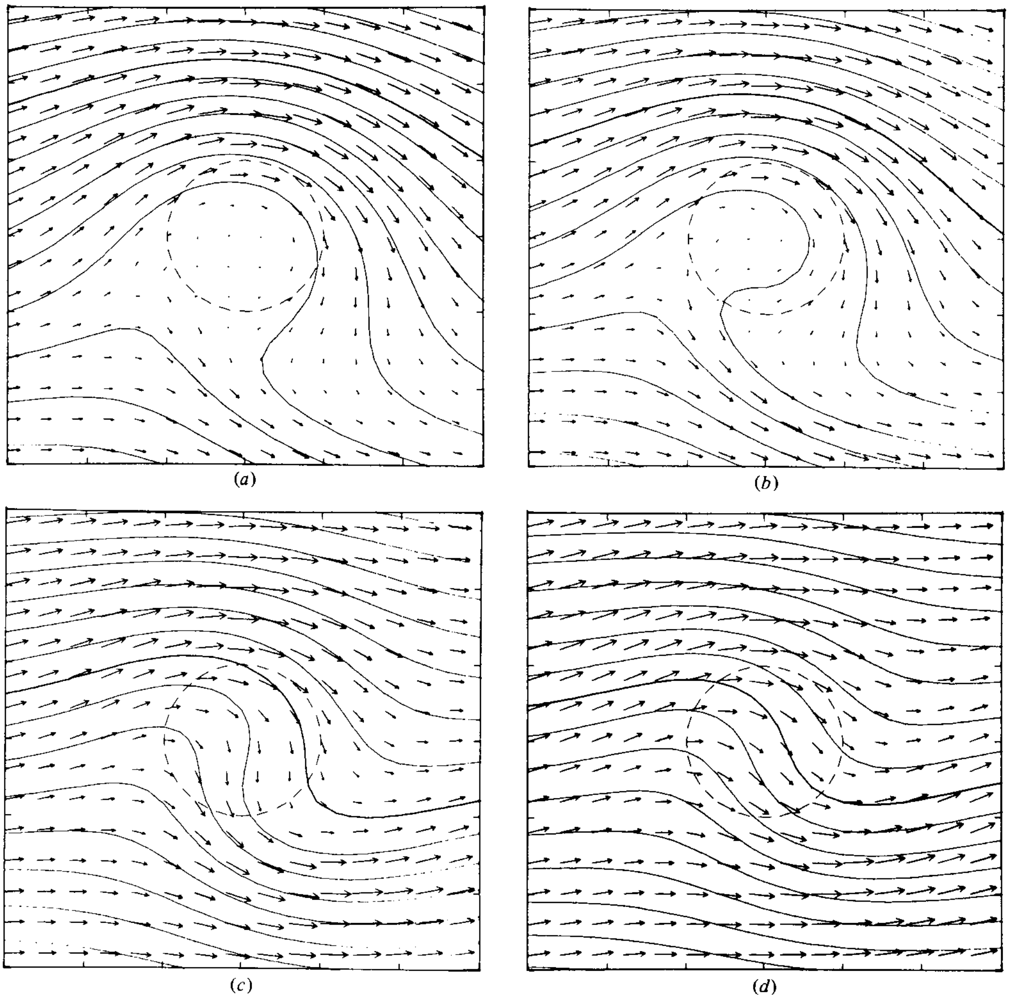

(*a*) (*b*) (*c*) (*d*)

FIGURE 6. Numerical solution as a function of γ_R for $\epsilon = 10^{-1}$, $\lambda = 10^{-1}$, and $\mu = 0{\cdot}522$. C.I. = 0·4. (*a*) $\gamma_R = 1{\cdot}0\times10^{-2}$, MV = 1·81. (*b*) $\gamma_R = 2{\cdot}0\times10^{-2}$, MV = 1·65. (*c*) $\gamma_R = 1{\cdot}0\times10^{-1}$, MV = 1·40. (*d*) $\gamma_R = 2{\cdot}0\times10^{-1}$, MV = 1·32.

γ_R	$B(1)$	$B(2)$	$B(3)$	$A(1)$	$A(2)$	$A(3)$	$\hat{C}_E$	$\hat{C}_T$
0·01	0·85	0·53	0·28	−6·57	−60·19	4·00	0·77	0·96
0·02	0·90	0·56	0·28	−3·87	24·72	2·06	0·78	0·65
0·10	0·78	0·38	0·18	3·92	0·58	0·32	0·90	0·26
0·20	0·55	0·25	0·12	0·19	0·13	0·11	0·96	0·13

TABLE 7. Blocking and asymmetry functions and drag coefficients as a function of γ_R for $\epsilon = 10^{-1}$, $\lambda = 10^{-1}$, and $\mu = 0{\cdot}522$.

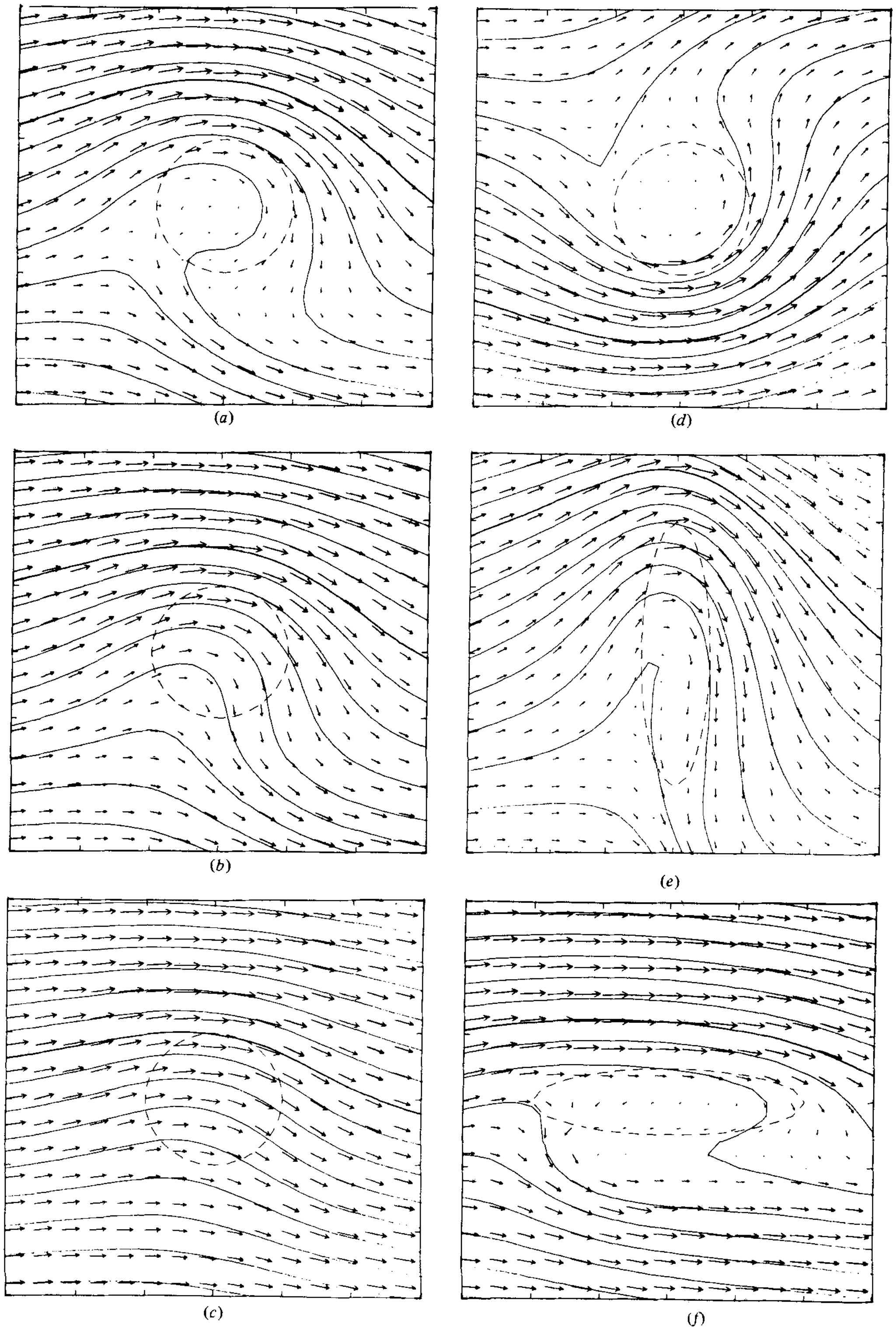

FIGURE 7. Numerical solutions with various obstacles for $\epsilon = 10^{-1}$, $\gamma_R = 2\cdot0 \times 10^{-2}$, $\lambda = 10^{-1}$, C.I. = 0·4. (*a*) $\mu = 2\mu_c$, MV = 1·65. (*b*) $\mu = \mu_c$, MV = 1·56. (*c*) $\mu = \frac{1}{2}\mu_c$, MV = 1·33. (*d*) $\mu = -2\mu_c$, MV = 1·72. (*e*) $\mu = 2\mu_c$ (prolate), MV = 1·90. (*f*) $\mu = 2\mu_c$ (oblate), MV = 1·33.

μ	$B(1)$	$B(2)$	$B(3)$	$A(1)$	$A(2)$	$A(3)$	$\hat{C}_E$	$\hat{C}_T$
$2\mu_c$	0·90	0·56	0·28	−3·87	24·72	2·06	0·78	0·65
μ_c	0·43	0·26	0·15	2·60	2·80	1·74	0·88	0·45
$\frac{1}{2}\mu_c$	0·13	0·07	0·04	0·47	0·65	0·58	0·97	0·14
$-2\mu_c$	0·71	0·41	0·24	−5·98§	−13·34§	7·62§	0·77	0·75
$2\mu_c$†	0·85	0·67	0·47	−10·56	−29·81	10·54	0·66	0·29
$2\mu_c$‡	0·74	0·33	0·16	−10·30	1·39	0·65	0·87	0·98

† Prolate obstacle (see figure 8*e*).

‡ Oblate obstacle (see figure 8*f*).

§ $A'(y) = 1/(A(y)+1)-1$ (see footnote in §5.1).

TABLE 8. Blocking and asymmetry functions and drag coefficients as a function of μ for $\epsilon = 10^{-1}$, $\gamma_R = 2{\cdot}0\times10^{-2}$, and $\lambda = 10^{-1}$.

The solution for $\gamma_R = 2{\cdot}0\times10^{-1}$ is quite close to the linear result (see table 2) despite the fact that the inertial terms are not inconsequential ($\epsilon/\gamma_R = 0{\cdot}5$). The solutions for $\gamma_R \sim \epsilon$ are in qualitative agreement with those of Vaziri & Boyer (1971). The major difference is that the latter do not include a non-divergent irrotational circulation of the type discussed by Huppert & Stern (1974) which causes the net shift of the streamlines to be zero.

The next series of experiments ascertains the effects of variations in the magnitude and shape of the topographic feature. For the parameter settings $\epsilon = 10^{-1}, \gamma_R = 2\times10^{-2}$, $\lambda = 10^{-1}$, $\hat{\beta} = 0$, and $u_\infty(y) = 1$, the results are summarized in figure 7 and table 8. As expected, reduction in the height of the obstacle from $2\mu_c$ to $\frac{1}{2}\mu_c$ results in decreased blocking, asymmetry, and total drag. The solution for $\mu = \mu_c$ should be compared with the inviscid results of figure 4(*a*) and tables 4 and 5. The former possesses a significantly greater blocking efficiency and a smaller left–right asymmetry. The centre of the region of stagnant fluid has been rotated $\sim 45°$ in a clockwise direction from its location in figure 4(*a*) because of the presence of bottom friction. As mentioned, figure 7(*c*) agrees well with quasi-geostrophic theory. In contrast figure 7(*a*) displays a strongly ageostrophic solution ($\mu \sim 5\epsilon$).

In agreement with the discussion of §5.1, a topographic depression (figure 7*d*) generates a cyclonic flow response. Finite ϵ results indicate that a stronger response is generated for $\mu = -0{\cdot}522$ than $\mu = 0{\cdot}522$. In addition frictional effects are diminished for $\mu < 0$ and enhanced for $\mu > 0$ [see (2.12)]. The combined effect of inertial and frictional terms is to produce a more inertial result with the associated larger asymmetry (table 8). Indeed figure 7(*d*) compares more favourably with the mirror image of figure 6(*a*) where γ_R is halved than with figure 7(*a*). The reduction in blocking efficiency for the depression case is also consistent with a decrease in viscous effect though the absence of a negative blocking is at variance with the inviscid results of §5.1.

Non-circularly symmetric obstacles are studied in figures 7(*e*) and (*f*) and table 8. For a prolate (oblate) feature, $\sigma_x = \frac{1}{2}(2)$ and $\sigma_y = 2(\frac{1}{2})$ in (2.13), and the volume of the obstacle is the same as for $\sigma_x = \sigma_y = 1$. An obstacle aligned normal to the inflow causes greater blocking and a more asymmetric response though the drag exerted on the flow is reduced due to its narrower zonal extent [see (3.6*b*)].

The effect of a change in the rotational Froude number λ (e.g. a change in g) is documented in table 9. In agreement with the analysis of §5.2 (table 5), the presence

λ	$B(1)$	$B(2)$	$B(3)$	$A(1)$	$A(2)$	$A(3)$	$\hat{C}_E$	$\hat{C}_T$
10^{-2}	0·902	0·563	0·288	−3·81	23·59	2·00	0·78	0·64
10^{-1}	0·897	0·556	0·281	−3·87	24·72	2·06	0·78	0·65

TABLE 9. Blocking and asymmetry functions and drag coefficients as a function of λ for $\epsilon = 10^{-1}$, $\gamma_R = 2{\cdot}0 \times 10^{-2}$, and $\mu = 0{\cdot}522$.

	$B(1)$	$B(2)$	$B(3)$	$A(1)$	$A(2)$	$A(3)$	$\hat{C}_E$	$\hat{C}_T$
$S = +\frac{1}{2}$	0·88	0·54	0·27	−3·69	−20·22	2·53	0·80	0·53
$S = -\frac{1}{2}$	0·89	0·54	0·28	−4·48	10·69	2·40	0·78	0·75
$y_c = +1$	0·98	0·67	0·41	−1·43	−1·86	−3·34	0·66	0·89
$y_c = 0$	1·00	0·78	0·59	−1·84	−4·97	−202·25	0·58	1·03
$y_c = -1$	1·04	0·82	0·43	0·61	10·39	1·27	0·66	0·84

TABLE 10. Blocking and asymmetry functions and drag coefficients for various $u_\infty(y)$ for $\epsilon = 10^{-1}$, $\gamma_R = 2{\cdot}0 \times 10^{-2}$, $\lambda = 10^{-1}$, and $\mu = 0{\cdot}522$.

of a free surface causes reduced blocking. In contrast the viscous results show increased flow asymmetry for increased λ. The reason for the increased drag lies in the greater deflexion of the free surface for larger λ.

Another set of experiments investigated the effect of variations in the horizontal structure of the zonal inflow. Results for inflow of the form

$$u_\infty(y) = 1{\cdot}0 + S\left(\frac{2}{\pi}\right)\tan^{-1} y,$$

are given in table 10. The fields are qualitatively similar to those in figure 5 (*d*) and are not shown. With anticyclonic shear ($S = +\frac{1}{2}$), the dominant flow is to the left of the obstacle. In contrast the cyclonic shear ($S = -\frac{1}{2}$) exhibits strong flow both to the left and to the right. When suitably non-dimensionalized (table 10), the asymmetry of the anticyclonic case is slightly greater. More surprisingly, the blocking efficiencies are virtually identical with each other and with the unsheared case (table 6). These results were confirmed by an inviscid, rigid-lid analysis similar to §5.1, but for flow with linear shear.

Results for jet-like inflows given by

$$u_\infty(y) = 0{\cdot}1 + 0{\cdot}9\,\mathrm{sech}^2\,(y - y_c),$$

are displayed in figure 8 and table 10. Here y_c denotes the location of the peak speed far upstream. For the jet centre to the left of the obstacle (figure 8 (*a*)), the dominant flow is to the left of the obstacle at $x = 0$ with weak return ($u < 0$) flow to the right. For $y_c = 0$ or $y_c = -1$, the flow is split by the obstacle. These results are similar to those of Nakamura (1978) using spherical geometry. As indicated in table 10, the blocking efficiency decreases for increasing y_c.

A final series of experiments (see table 11) incorporated the beta effect in the presence of a uniform inflow $u_\infty(y) = 1$. For $\hat{\beta} = +1$ (eastward flow), the solution (not shown) exhibits the well-known (e.g. Janowitz 1974; McCartney 1975) semicircular Rossby lee waves with wavelength $\sim 2\pi$. In agreement with Stevenson & Janowitz

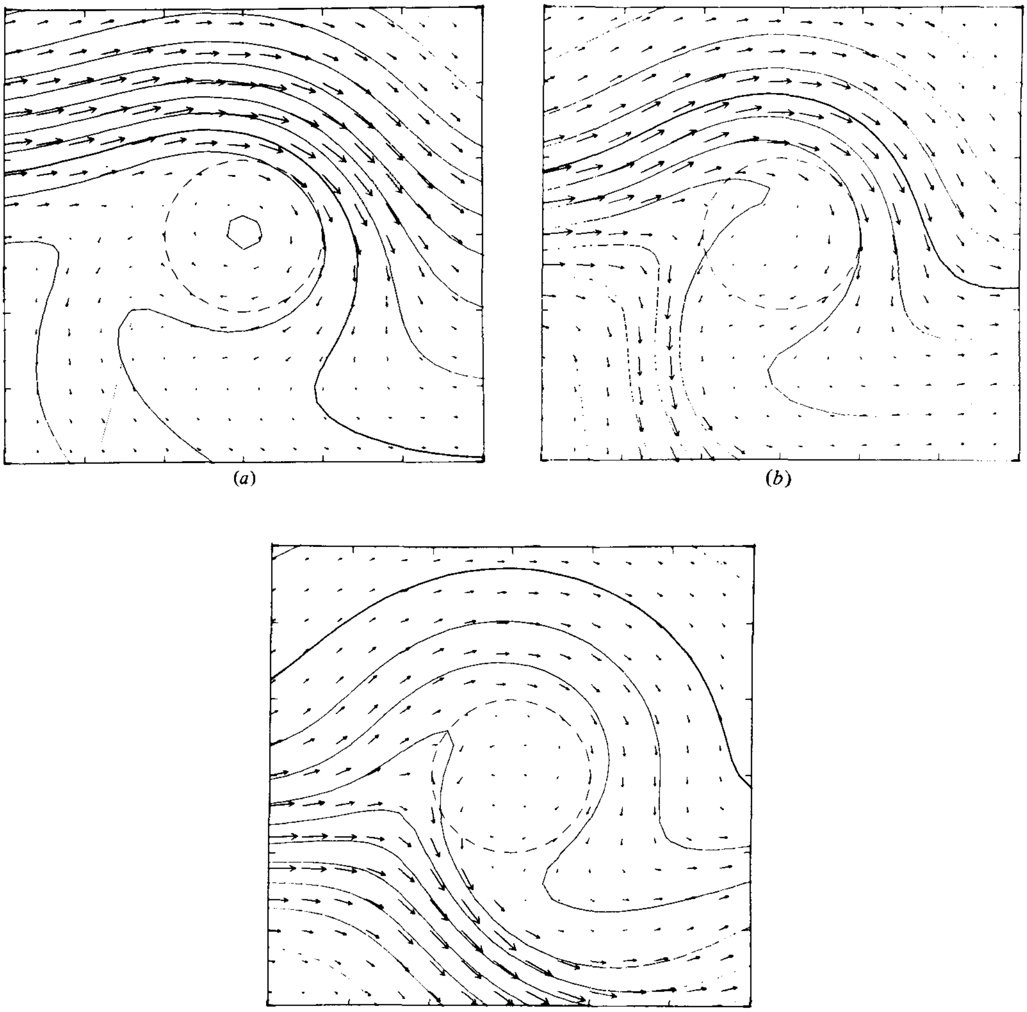

(*a*) (*b*)

(*c*)

FIGURE 8. Numerical solutions for inflow with jet profiles for $\epsilon = 10^{-1}$, $\gamma_R = 2{\cdot}0 \times 10^{-2}$, $\lambda = 10^{-1}$, and $\mu = 0{\cdot}522$. C.I. = 0·2. (*a*) $y_c = +1$, MV = 1·00. (*b*) $y_c = 0$, MV = 0·83. (*c*) $y_c = -1$, MV = 0·96.

$\hat{\beta}$	$B(1)$	$B(2)$	$B(3)$	$A(1)$	$A(2)$	$A(3)$	C_E	C_T
+1	0·95	0·40	0·06	−2·79	1·04	0·38	1·00	1·27
0	0·90	0·56	0·28	−3·87	24·72	2·06	0·78	0·65
−1	0·37	0·13	0·04	3·78	3·51	2·00	1·03	0·40

TABLE 11. Blocking and asymmetry functions and drag coefficients as a function of $\hat{\beta}$ for $\epsilon = 10^{-1}$, $\gamma_R = 2{\cdot}0 \times 10^{-2}$, $\lambda = 10^{-1}$, and $\mu = 0{\cdot}522$.

(1977), the waves decay downstream in a distance $O(2\epsilon/\gamma_R)$. For $\hat{\beta} = -1$ (westward flow), no lee waves are present, and the fields are similar to the $\hat{\beta} = 0$ case (figure 5*d*) and are not displayed. The presence of positive (negative) $\hat{\beta}$ rotates the stagnant region (counter) clockwise relative to the $\hat{\beta} = 0$ case. This effect results in increased (decreased) topographic drag. Table 11 also shows that the solution for $\hat{\beta} = +1$ has a stronger, though smaller, region of blocking compared to $\hat{\beta} = 0$ while the $\hat{\beta} = -1$ case is both weaker and smaller.

7. Conclusions

The flow of a rotating barotropic fluid over a finite isolated Gaussian obstacle has been studied. Emphasis has been placed on determining the blocking efficiency of the obstacle in various flow situations. Quasi-geostrophic theory (§4) indicates no blocking of the flow by the obstacle (i.e. just as much goes over as is incident on the obstacle). This deficiency arises because quasi-geostrophic theory restricts attention to non-divergent flow.

In this study the shallow water equations with a linear Rayleigh friction were used to determine the blocking. The approach is valid in the limit $(\gamma^{\frac{1}{2}}, \epsilon\mu\delta^2, \gamma\mu\delta^2) \rightarrow 0$. Linear viscous results (§3) indicate 100 % blocking efficiency when $\mu \gg \gamma_R (\sim \gamma^{\frac{1}{2}})$. In contrast inviscid inertial theory (§5) indicates a blocking efficiency of ~ 10 % which is independent of the Rossby number ϵ. It was shown that the presence of a free surface decreases the blocking for inertial flow when $\epsilon \ll 1$ but has no effect on linear viscous or quasi-geostrophic flow.

Numerical solutions of the full model equations (§6) confirm and extend these conclusions. In particular, the inclusion of weak friction in inertial flow increases the blocking efficiency which is a maximum for small but finite values of dissipation. The presence of horizontal shear in the upstream inflow does not significantly change the blocking efficiency of the obstacle. Jet-like inflows whose peaks speed is on-line with or to the right of the obstacle centre are split by the obstacle and are more strongly blocked than jets to the left of centre. Lastly, on the beta plane, the blocking is greater for eastward rather than westward flow.

The author thanks Dr Akira Kasahara for fruitful discussions during the course of this investigation. John C. Adams kindly provided the FORTRAN code used to solve the finite-difference version of the elliptic equation of §3 by direct matrix inversion.

REFERENCES

ARAKAWA, A. & LAMB, V. R. 1977 The U.C.L.A. general circulation model. In *General Circulation Models of the Atmosphere*, pp. 173–265. Academic.

BANNON, P. R. 1979 On the dynamics of the East African jet. Ph.D. thesis, University of Colorado, Boulder.

BUZZI, A. & TIBALDI, S. 1977 *Quart. J. Roy. Met. Soc.* **103**, 135–150.

CHARNEY, J. G. 1955 *Proc. Nat. Acad. Sci.* **41**, 731–740.

COTTRELL, J. R. 1970 Is the great red spot on Jupiter a Taylor column in horizontal shear flow? *Woods Hole Oceanographic Institution GFD Summer Program Notes.*

EDELMANN, W. 1972 *Beitr. z. Phys. der Atmos.* **45**, 196–229.

HIDE, R. 1961 *Nature* **190**, 895–896.

HIDE, R. 1971 *J. Fluid Mech.* **49**, 745–751.

HIDE, R. & IBBETSON, A. 1966 *Icarus* **5**, 279–290.

HOGG, N. G. 1973*a* *J. Fluid Mech.* **58**, 517–537.

HOGG, N. G. 1973*b* *Deep-Sea Res.* **20**, 449–459.

HUPPERT, H. E. 1975 *J. Fluid Mech.* **67**, 397–412.

HUPPERT, H. E. & BRYAN, K. 1976 *Deep-Sea Res.* **23**, 655–679.

HUPPERT, H. E. & STERN, M. E. 1974 *J. Fluid Mech.* **64**, 417–436.

INGERSOLL, A. P. 1969 *J. Atmos. Sci.* **26**, 744–752.

JACOBS, S. J. 1964 *J. Fluid Mech.* **20**, 581–591.

JANOWITZ, G. S. 1974 *J. Fluid Mech.* **66**, 455–464.

JOHNSON, E. R. 1978*a* *J. Fluid Mech.* **86**, 209–224.

JOHNSON, E. R. 1978*b* *Geophys. Astrophys. Fluid Dyn.* **9**, 327–329.

KASAHARA, A. 1966 *J. Atmos. Sci,* **23**, 259–271.

MCCARTNEY, M. S. 1975 *J. Fluid Mech.* **68**, 71–95.

MCINTYRE, M. E. 1972 *J. Fluid Mech.* **52**, 209–243.

MERKINE, L. & KALNAY-RIVAS, E. 1976 *J. Atmos. Sci.* **33**, 908–922.

MIYAKODA, K. 1973 *Proc. Roy. Irish Acad.* **73***A*, 99–130.

NAKAMURA, H. 1978 *J. Meteor. Soc. Japan* **56**, 317–367.

ORLANSKI, I. 1976 *J. Comput. Phys.* **21**, 251–269.

PIACSEK, S. A. & WILLIAMS, G. P. 1970 *J. Comput. Phys.* **6**, 392–405.

PROUDMAN, J. 1916 *Proc. Roy. Soc.* A **92**, 408–424.

ROBERTS, D. G., HOGG, N. G., BISHOP, D. G. & FLEWELLEN, C. G. 1974 *Deep-Sea Res.* **21**, 175–184.

SMITH, G. D. 1975 *Numerical Solution of Partial Differential Equations.* Oxford University Press.

STEVENSON, J. W. & JANOWITZ, G. S. 1977 *Dyn. Atmos. Oceans* **1**, 225–239.

STEWARTSON, K. 1957 *J. Fluid Mech.* **3**, 17–26.

STONE, P. H. & BAKER, D. J. 1968 *Quart. J. Roy. Met. Soc.* **94**, 576–580.

TAYLOR, G. I. 1923 *Proc. Roy. Soc.* A **104**, 213–218.

TAYLOR, G. I. 1921 *Proc. Roy. Soc.* A **100**, 114–121.

VAZIRI, A. & BOYER, D. L. 1971 *J. Fluid Mech.* **50**, 79–95.

VERGEINER, I. & OGURA, Y. 1972 *J. Atmos. Sci.* **29**, 270–284.

WILLIAMS, G. P. 1969 *J. Fluid Mech.* **37**, 727–750.